

Susceptibility of F/A-18 Flight Controllers to the Falling-Leaf Mode: Nonlinear Analysis

Abhijit Chakraborty,* Peter Seiler,† and Gary J. Balas‡
University of Minnesota, Minneapolis, Minnesota 55455

DOI: 10.2514/1.50675

The F/A-18 Hornet aircraft with the original flight control law exhibited a nonlinear out-of-control phenomenon known as the falling-leaf mode. This unstable mode was suppressed by modifying the original control law. This paper employs the falling-leaf phenomenon as an example to demonstrate the utility of recently developed nonlinear analysis methods to flight control validation tools. The flight control law is usually validated and verified by performing linear robustness analysis at different trim points and running many Monte Carlo simulations. Additional insight can be gained by using nonlinear analyses. This paper compares the two flight control laws using nonlinear region-of-attraction analyses and Monte Carlo simulations. The results of these nonlinear analyses indicate that the revised flight control law has significantly improved nonlinear robustness properties as compared with baseline design.

Nomenclature

a_y	= lateral acceleration, g
g	= gravitational constant, $\frac{\text{ft}}{\text{s}^2}$
m	= mass, slugs
p	= roll rate, $\frac{\text{rad}}{\text{s}}$
q	= pitch rate, $\frac{\text{rad}}{\text{s}}$
\bar{q}	= dynamic pressure, $\frac{\text{lbs}}{\text{ft}^2}$
r	= yaw rate, $\frac{\text{rad}}{\text{s}}$
T	= thrust, lbf
V	= velocity, $\frac{\text{ft}}{\text{s}}$
α	= angle of attack, rad
β	= sideslip angle, rad
θ	= pitch angle, rad
ρ	= density, $\frac{\text{slugs}}{\text{ft}^3}$
ϕ	= bank angle, rad
ψ	= yaw angle, rad

I. Introduction

SAFETY critical flight systems require extensive validation before entry into service. Validation of the flight control system is becoming more difficult due to the increased use of advanced flight control algorithms, e.g., nonlinear flight controls systems. NASA's Aviation Safety Program aims to reduce the fatal (commercial) aircraft accident rate by 90% by 2022 [1]. A key challenge to achieving this goal is the need for improved validation and certification tools for the flight systems. The current certification and validation procedure involves analysis, simulations, and experimental techniques such as flight tests [1]. Before flight tests, extensive analyses and simulations are performed to validate safety of the system. Standard practice is to assess the closed-loop stability and performance characteristics of the aircraft flight control system around numerous trim conditions using linear analysis tools. These

techniques include stability margins, robustness analyses and worst-case analyses. Linear analyses techniques are supplemented with Monte Carlo simulations of the full nonlinear equations of motion to provide further confidence in the system performance. These simulations are also used to uncover nonlinear dynamic characteristics, e.g., limit cycles, that are not revealed by the linear analyses. Hence, current practice involves extensive linear analyses at different trim conditions and probabilistic nonlinear simulations. The certification process typically does not involve nonlinear analysis methods.

Recently, significant research has been performed on the development of nonlinear analysis tools for computing regions of attraction, reachability sets, input-output gains, and robustness with respect to uncertainty for nonlinear polynomial systems [2–11]. These tools make use of polynomial sum-of-squares (SOS) optimization [11] and hence they can only be applied to systems whose dynamics are described by polynomial vector fields. These techniques offer great potential to complement the linear analyses and nonlinear simulations that are typically used in the flight control validation process.

The main objective of this paper is to use nonlinear region-of-attraction (ROA) analyses and Monte Carlo simulations to assess the robustness properties of two F/A-18 flight control laws. ROA analysis for nonlinear systems provides a guaranteed stability region using Lyapunov theory and SOS optimization [2–4, 11, 12]. The ROA analysis complements the use of Monte Carlo simulations. SOS stability analysis has previously been applied to simple examples [2–4, 11, 12]. This paper presents the first successful application of these techniques to a flight control problem of realistic complexity.

The analysis of the F/A-18 control laws is a particularly interesting example for the application of nonlinear robustness analysis techniques. The U.S. Navy F/A-18 A/B/C/D Hornet aircraft with the baseline flight control law experienced a number of out-of-control flight departure phenomenon known as the falling-leaf mode [13, 14]. An extensive revision of the original (baseline) flight control law was performed by NAVAIR and Boeing in 2001 to suppress the falling-leaf departure phenomenon [14]. The revised control law was implemented and successfully flight tested on the F/A-18 E/F Super Hornet aircraft, which has similar aerodynamic and inertial characteristics as of the Hornet [14].

The falling-leaf mode is nonlinear in nature and was handled by modifying the flight control law in the Hornet. Accurate modeling of the falling-leaf mode is still an open issue [15] and this is a significant factor in the inability to predict the susceptibility of an aircraft to this mode. However, this mode is inherently nonlinear and hence it provides a good example for nonlinear analysis methods. The F/A-18 mathematical model of used in this paper is able to reproduce a falling-leaf type of motion. Linear analyses have been performed on

Presented as Paper 2009-5675 at the AIAA Guidance, Navigation, and Control Conference, Chicago IL, 10–13 August 2009; received 7 May 2010; revision received 3 August 2010; accepted for publication 6 September 2010. Copyright © 2010 by Abhijit Chakraborty, Peter Seiler, Gary J. Balas. Published by the American Institute of Aeronautics and Astronautics, Inc., with permission. Copies of this paper may be made for personal or internal use, on condition that the copier pay the \$10.00 per-copy fee to the Copyright Clearance Center, Inc., 222 Rosewood Drive, Danvers, MA 01923; include the code 0731-5090/11 and \$10.00 in correspondence with the CCC.

*Graduate Research Assistant, Department of Aerospace Engineering and Mechanics; chakrab@aem.umn.edu.

†Senior Research Associate, Department of Aerospace Engineering and Mechanics; seiler@aem.umn.edu.

‡Professor, Department of Aerospace Engineering and Mechanics; balas@aem.umn.edu. Associate Fellow AIAA.

both the flight controllers of the Hornet [16,17]. Classical gain and phase margin analyses indicate that the revised flight control law has similar robustness properties as the baseline flight control law. More advanced linear analysis tools, such as μ and worst-case performance, indicate that the revised flight controller has noticeably better robustness properties than the baseline control law [16,17]. However, it can be difficult to interpret these results because the falling-leaf motion is a truly nonlinear dynamic phenomenon. Thus nonlinear analyses tools would provide useful insight into why the revised design is robust to the falling-leaf motion while the baseline design is susceptible.

The paper has the following structure. First, a computational procedure to estimate regions of attraction for polynomial systems [2–4,18–21] is provided in Sec. II. The six-degree-of-freedom (DOF) nine-state model of the F/A-18 aircraft is discussed in Sec. III. State-space realizations for the baseline and revised control laws are given in Sec. IV. Polynomial models are constructed in Sec. V for the closed-loop systems with the baseline and revised flight control laws. This step is required because the proposed computational method to estimate the ROA is only applicable to polynomial systems. The robustness properties of the two closed-loop systems are then analyzed in Sec. VI. The paper concludes with a summary of the contributions of the paper.

II. ROA Estimation

This section describes the technical approach to estimate the ROA for nonlinear, polynomial systems. This analysis is based on a fundamental difference between asymptotic stability for linear and nonlinear systems. For linear systems, asymptotic stability of an equilibrium point is a global property. In other words, if an equilibrium point is asymptotically stable then its state trajectory will converge back to the equilibrium when starting from any initial condition. For nonlinear systems, asymptotically stable equilibrium points are not necessarily globally asymptotically stable. Khalil [22] and Vidyasagar [23] provide good introductory discussions of this issue. The ROA of an asymptotically stable equilibrium point is the set of initial conditions whose state trajectories converge back to the equilibrium [22]. If the ROA is small, then a disturbance can easily drive the system out of the ROA and the system will fail to come back to the stable equilibrium point. Thus the size of the ROA can be interpreted as a measure of the stability properties of a nonlinear system around an equilibrium point. This motivates the computation of ROA estimates.

Consider an autonomous nonlinear, polynomial system of the form

$$\dot{x} = f(x), \quad x(0) = x_0 \quad (1)$$

where $x \in \mathbb{R}^n$ is the state vector and $f: \mathbb{R}^n \rightarrow \mathbb{R}^n$ is a multivariable polynomial. Assume that the origin is a locally asymptotically stable equilibrium point. This assumption is without loss of generality because state coordinates can always be redefined to shift an equilibrium point to the origin. The ROA is formally defined as

$$\mathcal{R} := \{x_0 \in \mathbb{R}^n: \text{If } x(0) = x_0 \text{ then } \lim_{t \rightarrow \infty} x(t) = 0\} \quad (2)$$

Computing the exact ROA for nonlinear dynamic systems is very difficult. There has been significant research devoted to estimating invariant subsets of the ROA [5–11,24,25]. The approach taken in this paper is to restrict the search to ellipsoidal approximations of the ROA. Given an $n \times n$ matrix $N = N^T > 0$, define the shape function $p(x) := x^T N x$ and level set $\mathcal{E}_\beta := \{x \in \mathbb{R}^n: p(x) \leq \beta\}$. $p(x)$ defines the shape of the ellipsoid and β determines the size of the ellipsoid \mathcal{E}_β . The choice of p is problem dependent and reflects dimensional scaling information as well as the importance of certain directions in the state space. N can typically be chosen to be diagonal with $N_{i,i} := 1/x_{i,\max}^2$. With this choice, $\mathcal{E}_{\beta=1}$ is a coordinate-aligned ellipsoid whose extreme points along the i th state direction are $\pm x_{i,\max}$. In this form, the level set value β provides an easily interpretable value for the size of the level set.

Given the shape function p , the problem is to find the largest ellipsoid \mathcal{E}_β contained in the ROA:

$$\beta^* = \max \beta \quad \text{subject to: } \mathcal{E}_\beta \subset \mathcal{R} \quad (3)$$

Determining the best ellipsoidal approximation to the ROA is still a challenging computational problem. Instead, lower and upper bounds for β^* satisfying $\underline{\beta} \leq \beta^* \leq \bar{\beta}$ are computed. If the lower and upper bounds are close then the largest ellipsoid level set, defined by Eq. (3), has been approximately computed.

The upper bounds are computed via a search for initial conditions leading to divergent trajectories. If $\lim_{t \rightarrow \infty} x(t) = +\infty$ when starting from $x(0) = x_{0,\text{div}}$ then $x_{0,\text{div}} \notin \mathcal{R}$. If we define $\bar{\beta}_{\text{div}} := p(x_{0,\text{div}})$ then $\mathcal{E}_{\bar{\beta}_{\text{div}}} \not\subset \mathcal{R}$ which implies $\beta^* \leq \bar{\beta}_{\text{div}}$. An exhaustive Monte Carlo search is used to find a tight upper bound on β^* . Specifically, random initial conditions are chosen starting on the boundary of a large ellipsoid: x_0 is chosen to satisfy $p(x_0) = \beta_{\text{try}}$ where β_{try} is sufficiently large that $\beta_{\text{try}} \gg \beta^*$. If a divergent trajectory is found, the initial condition is stored and an upper bound on β^* is computed. β_{try} is then decreased by a factor of 0.995 and the search continues until a maximum number of simulations is reached. There is a tradeoff involved in choosing the factor 0.995. A smaller factor results in a larger reduction of the upper bound for each divergent trajectory but it typically limits the accuracy of the upper bound. No divergent trajectories can be found when $\beta_{\text{try}} < \beta^*$ and this roughly limits the upper bound accuracy to $\beta^*/(\text{factor})$. The value of 0.995 is very close to one and is chosen to obtain an accurate upper bound on β^* . $\bar{\beta}_{\text{MC}}$ will denote the smallest upper bound computed with this Monte Carlo search.

The lower bounds are computed using Lyapunov functions and recent results connecting sums-of-squares polynomials to semi-definite programming. Computing these bounds requires the vector field $f(x)$ in Eq. (1) to be a polynomial function. The computational algorithm is briefly described here and full algorithmic details are provided in references [2–4,18–21]. Lemma 1 is the main Lyapunov theorem used to compute lower bounds on β^* . This specific lemma is proved by [2] but very similar results are given in textbooks [23].

Lemma 1: if there exists $\gamma > 0$ and a polynomial $V: \mathbb{R}^n \rightarrow \mathbb{R}$ such that

$$V(0) = 0 \quad \text{and} \quad V(x) > 0 \quad \forall x \neq 0 \quad (4)$$

$$\Omega_\gamma := \{x \in \mathbb{R}^n: V(x) \leq \gamma\} \text{ is bounded} \quad (5)$$

$$\Omega_\gamma \subset \{x \in \mathbb{R}^n: \nabla V(x)f(x) < 0\} \cup \{0\} \quad (6)$$

then for all $x \in \Omega_\gamma$, the solution of Eq. (1) exists, satisfies $x(t) \in \Omega_\gamma$ for all $t \geq 0$, and $\Omega_\gamma \subset \mathcal{R}$.

A function V , satisfying the conditions in Lemma 1 is a Lyapunov function and Ω_γ provides an estimate of the ROA. If $x = 0$ is asymptotically stable, a linearization can be used to compute a Lyapunov function. Let $A := \frac{\partial f}{\partial x}|_{x=0}$ be the linearization of the dynamics about the origin and compute $P > 0$ that solves the Lyapunov equation $A^T P + P A = -I$. $V_{\text{LIN}}(x) := x^T P x$ is a quadratic Lyapunov function that satisfies the conditions of Lemma 1 for sufficiently small $\gamma > 0$. V_{LIN} can be used to compute a lower bound on β^* by solving two maximizations:

$$\gamma^* := \max \gamma \quad \text{subject to: } \Omega_\gamma \subset \{x \in \mathbb{R}^n: \nabla V_{\text{LIN}}(x)f(x) < 0\} \quad (7)$$

$$\underline{\beta} := \max \beta \quad \text{subject to: } \mathcal{E}_\beta \subset \Omega_{\gamma^*} \quad (8)$$

The first maximization finds the largest level set Ω_{γ^*} of V_{LIN} such that Lemma 1 can be used to verify $\Omega_{\gamma^*} \subseteq \mathcal{R}$. The second maximization finds the largest ellipsoid \mathcal{E}_β contain within Ω_{γ^*} . The set containment constraints are replaced with a sufficient condition involving non-negative polynomials [2]. For example, $\mathcal{E}_\beta \subset \Omega_{\gamma^*}$ in Optimization (8) is replaced by

$$\underline{\beta} := \max_{\beta, s(x)} \beta \quad \text{subject to: } s(x) \geq 0$$

$$\forall x - (\beta - p(x))s(x) + (\gamma^* - V_{\text{LIN}}(x)) \geq 0 \quad \forall x \quad (9)$$

The function $s(x)$ is a decision variable of the optimization, i.e., it is found as part of the optimization. It is straight-forward to show that the two nonnegativity conditions in Optimization (9) are a sufficient condition for the set containment condition in Optimization (8). If $s(x)$ is restricted to be a polynomial, both constraints involve the nonnegativity of polynomial functions. A sufficient condition for a generic multivariate polynomial $h(x)$ to be nonnegative is the existence of polynomials $\{g_1, \dots, g_n\}$ such that $h = g_1^2 + \dots + g_n^2$. A polynomial which can be decomposed in this way is called a SOS. Finally, if we replace the nonnegativity conditions in Optimization (9) with SOS constraints, then we arrive at an SOS optimization problem:

$$\underline{\beta} := \max \beta \quad \text{subject to: } s(x) \text{ is SOS} - (\beta - p(x))s(x)$$

$$+ (\gamma^* - V_{\text{LIN}}(x)) \text{ is SOS} \quad (10)$$

There are connections between SOS polynomials and semidefinite matrices. Moreover, optimization problems involving SOS constraints can be converted and solved as a semidefinite programming optimization. Importantly, there is freely available software to set up and solve these problems [12,26–28]. $\underline{\beta}_{\text{LIN}}$ will denote the lower bound obtained from Optimization (10) using the quadratic Lyapunov function obtained from linearized analysis.

Unfortunately, $\underline{\beta}_{\text{LIN}}$ is usually orders of magnitude smaller than the upper bound β_{MC} . Several methods to compute better Lyapunov functions exist, including $V-s$ iterations [18–21], bilinear optimization [2], and the use of simulation data [3,4]. In this paper, $V-s$ iteration is used to compute the Lyapunov function and the inner ellipsoidal approximation to the ROA. The Lyapunov function $V(x)$ in the iteration is initialized with the linearized Lyapunov function V_{LIN} . The iteration also uses functions $l_1(x) = -\epsilon_1 x^T x$ and $l_2(x) = -\epsilon_2 x^T x$ where ϵ_1 and ϵ_2 are small positive constants on the order of 10^{-6} . The $V-s$ iteration algorithm steps are as follows:

1) γ step: hold V fixed and solve for s_2 and γ^* :

$$\gamma^* := \max_{s_2 \in \text{SOS}, \gamma} \gamma \quad \text{s.t.} \quad -(\gamma - V)s_2 - \left(\frac{\partial V}{\partial x} f + l_2 \right) \in \text{SOS}$$

2) β step: hold V , γ^* fixed and solve for s_1 and $\underline{\beta}$:

$$\underline{\beta} := \max_{s_1 \in \text{SOS}, \beta} \beta \quad \text{s.t.} \quad -(\beta - p)s_1 + (\gamma^* - V) \in \text{SOS}$$

3) V step: hold $s_1, s_2, \underline{\beta}, \gamma^*$ fixed and solve for V satisfying

$$-(\gamma^* - V)s_2 - \left(\frac{\partial V}{\partial x} f + l_2 \right) \in \text{SOS}$$

$$-(\underline{\beta} - p)s_1 + (\gamma^* - V) \in \text{SOS} \quad V - l_1 \in \text{SOS}, \quad V(0) = 0$$

4) Repeat as long as the lower bound $\underline{\beta}$ continues to increase.

Software and additional documentation on the $V-s$ iteration is provided in the [28]. The basic issue is that searching for a Lyapunov function V results in a bilinear term Vs_2 in the γ constraint. This bilinear term can not be handled directly within the SOS programming framework because the constraints in SOS programs must be linear in the decision variables. The $V-s$ iteration avoids the bilinearity in Vs_2 by holding either s_2 or V fixed. Each step of this iteration is a linear SOS optimization that can be solved with available software. In the $V-s$ iteration, the Lyapunov functions are allowed to have polynomial degree greater than two. Increasing the degree of the Lyapunov function will improve the lower bound at the expense of computational complexity.

The V step requires additional discussion. An interior-point linear matrix inequality solver is used to find a feasible solution to the feasibility problem in the V step. The Lyapunov function V that is used in the γ and β steps will be feasible for the constraints in the V

step. Thus it is possible for the solver to simply return the same Lyapunov function that was used in the γ and β steps. While this is possible, it typically happens that the solver returns a different V that allows both γ and β to be increased at the next iteration. This step can be understood by the fact that interior-point solvers try to return a solution at the analytic center of set specified by the linear matrix inequality constraints. Thus the V step typically returns a feasible V that is “pushed away” from the constraints. A more formal theory for the behavior of this feasibility step is an open question.

III. F/A-18 Aircraft and Model Development

A nonlinear mathematical model of the F/A-18 Hornet aircraft including its aerodynamic characteristics and control surface description is presented for the purpose of linear and nonlinear analysis of flight control system. Unfortunately, a full aerodynamic data set for the Hornet is not available in the public domain. Hence, a nonlinear model of the F/A-18 aircraft is developed based on the publicly available aerodynamic data for the F/A-18 High-Alpha Research Vehicle (HARV) [29–34]. The model developed for analysis has limitations. First, the flight test data are provided over a range of 5 or 10° to 60° angle-of-attack with fewer data points at low angle-of-attack ($0^\circ \leq \alpha \leq 10^\circ$). Extrapolation of data within the lower range of angle-of-attack can lead to unrealistic fits which may lead to unrealistic aerodynamic characteristics at low angle-of-attack. For traditional aircraft, the aerodynamic characteristics of the vehicle do not change significantly at low angle-of-attack ($\alpha \leq 10^\circ$). Hence if data are unavailable, the aerodynamic coefficient is held constant for angle-of-attack between 0 and 10° .[§] The resulting model is reasonably accurate for an angle-of-attack range from 0° – 60° . Second, data are unavailable for nonzero sideslip flight conditions. However, the basic airframe coefficients are functionally dependent on both α, β . In this paper, the basic airframe dependence of $C_{Y,\text{basic}}(\alpha, \beta)$, $C_{l,\text{basic}}(\alpha, \beta)$, $C_{n,\text{basic}}(\alpha, \beta)$ are approximated as $C_{Y,\text{basic}}(\alpha)\beta$, $C_{l,\text{basic}}(\alpha)\beta$, $C_{n,\text{basic}}(\alpha)\beta$ to account for this lack of data. This implies, for C_Y , that the sideforce is expected to be zero when the sideslip is zero. This approximation step can also be viewed as linearization of the sideslip effect around the origin. A similar approach to approximate sideforce was considered by Stevens and Lewis [35]. Note that the sideslip characteristics are an important aspect of the falling-leaf motion. The nonlinear aircraft model used in this paper is able to reproduce a falling-leaf motion even with the approximations specified preceding.

The mathematical description of the six-DOF, nine-state model for the F/A-18 aircraft uses flight tests data publicly available for the F/A-18 HARV [29–33]. The aerodynamic characteristics of the F/A-18 Hornet and Super Hornet are similar to the HARV aircraft. The aerodynamic characteristics of the aircraft are expressed as closed-form polynomial approximations to flight test data with functional dependence on states and control surfaces [16,17]. State variables describing the F/A-18 mathematical model are: velocity (V , ft/s), sideslip angle (β , rad), angle-of-attack (α , rad), roll rate (p , rad/s), pitch rate (q , rad/s), yaw rate (r , rad/s), bank angle (ϕ , rad), pitch angle (θ , rad) and yaw angle (ψ , rad). Symmetric stabilator (δ_{stab} , rad), differential aileron (δ_{ail} , rad), differential rudder (δ_{rud} , rad) and thrust (T , lbf) are considered as control effectors for the analyses performed in this paper. Table 1 lists the aerodynamic reference and physical parameters of the F/A-18 Hornet [36].

The mathematical model of the F/A-18 Hornet is described by the conventional aircraft equations of motion [33,37,38] in the following form:

$$\dot{x} = f(x, u) \quad (11)$$

where $x := [V(\text{ft/s}), \beta(\text{rad}), \alpha(\text{rad}), p(\text{rad/s}), q(\text{rad/s}), r(\text{rad/s}), \phi(\text{rad}), \theta(\text{rad}), \psi(\text{rad})]$, and $u := [\delta_{\text{ail}}(\text{rad}), \delta_{\text{rud}}(\text{rad}), \delta_{\text{stab}}(\text{rad}), T(\text{lbf})]$.

[§]Personal communication with Dr. John V. Foster, NASA Langley Research Center.

Table 1 Aircraft parameters

Parameter	Symbol	Value
Wing area	S	400 ft ²
Mean aerodynamic chord	\bar{c}	11.52 ft
Wing span	b	37.42 ft
Mass	m	1034.5 slug
Roll axis moment of inertia	I_{xx}	23,000 slug · ft ²
Pitch axis moment of inertia	I_{yy}	151,293 slug · ft ²
Yaw axis moment of inertia	I_{zz}	169,945 slug · ft ²
Cross product of inertia about y-axis	I_{xz}	-2971 slug · ft ²

The equations of motion are presented next. Closed-form polynomial expressions for the aerodynamic coefficients are presented in Appendix A. A detailed description of the aerodynamic model is provided in [16,17].

The kinematics of the aircraft are described in terms of Euler angles. The kinematic relations are given in Eq. (12):

$$\begin{bmatrix} \dot{\phi} \\ \dot{\theta} \\ \dot{\psi} \end{bmatrix} = \begin{bmatrix} 1 & \sin \phi \tan \theta & \cos \phi \tan \theta \\ 0 & \cos \phi & -\sin \phi \\ 0 & \sin \phi \sec \theta & \cos \phi \sec \theta \end{bmatrix} \begin{bmatrix} p \\ q \\ r \end{bmatrix} \quad (12)$$

Equation (13) defines the force equations for the F/A-18 Hornet. The aerodynamic forces, gravity forces and thrust force applied to the aircraft are considered. For all analyses, the thrust force is assumed to be constant and fixed at its trim value:

$$\begin{aligned} \dot{V} = & -\frac{1}{m}(D \cos \beta - Y \sin \beta) + g(\cos \phi \cos \theta \sin \alpha \cos \beta \\ & + \sin \phi \cos \theta \sin \beta - \sin \theta \cos \alpha \cos \beta) \\ & + \frac{T}{m} \cos \alpha \cos \beta \end{aligned} \quad (13a)$$

$$\begin{aligned} \dot{\alpha} = & -\frac{1}{mV \cos \beta} L + q - \tan \beta (p \cos \alpha + r \sin \alpha) \\ & + \frac{g}{V \cos \beta} (\cos \phi \cos \theta \cos \alpha + \sin \alpha \sin \theta) - \frac{T \sin \alpha}{mV \cos \beta} \end{aligned} \quad (13b)$$

$$\begin{aligned} \dot{\beta} = & \frac{1}{mV} (Y \cos \beta + D \sin \beta) + p \sin \alpha - r \cos \alpha \\ & + \frac{g}{V} \cos \beta \sin \phi \cos \theta \\ & + \frac{\sin \beta}{V} \left(g \cos \alpha \sin \theta - g \sin \alpha \cos \phi \cos \theta + \frac{T}{m} \cos \alpha \right) \end{aligned} \quad (13c)$$

where C_D , C_L , C_Y denote the drag, lift and sideforce coefficients, respectively. These force coefficients are expressed as a sum of basic airframe and control deflections as $C_* = C_{*,\text{basic}}(\alpha, \beta) + C_{*,\text{control}}(\alpha, \delta_{\text{control}})$. The variable $*$ denotes D , L , Y and δ_{control} can be replaced by δ_{stab} , δ_{ail} , δ_{rud} . The detailed expressions for these force coefficients are provided in Tables 2 and 3.

The aerodynamic moments are considered for external applied moments. The gyroscopic effect of the moment is neglected in this paper. Equation (14) describes the moment equations for the F/A-18 Hornet:

$$\begin{bmatrix} \dot{p} \\ \dot{q} \\ \dot{r} \end{bmatrix} = \begin{bmatrix} \frac{I_{xz}}{\kappa} & 0 & \frac{I_{xz}}{\kappa} \\ 0 & \frac{1}{I_{yy}} & 0 \\ \frac{I_{xz}}{\kappa} & 0 & \frac{I_{xz}}{\kappa} \end{bmatrix} \times \left(\begin{bmatrix} l \\ M \\ n \end{bmatrix} - \begin{bmatrix} 0 & -r & q \\ r & 0 & -p \\ -q & p & 0 \end{bmatrix} \begin{bmatrix} I_{xx} & 0 & -I_{xz} \\ 0 & I_{yy} & 0 \\ -I_{xz} & 0 & I_{zz} \end{bmatrix} \begin{bmatrix} p \\ q \\ r \end{bmatrix} \right) \quad (14)$$

Table 2 Aerodynamic moment coefficients

Pitching moment	Rolling moment	Yawing moment
$C_{m_{\alpha_2}} = -1.2897$	$C_{l_{\beta_4}} = -1.6196$	$C_{n_{\beta_2}} = -0.3816$
$C_{m_{\alpha_1}} = 0.5110$	$C_{l_{\beta_3}} = 2.3843$	$C_{n_{\beta_1}} = 0.0329$
$C_{m_{\alpha_0}} = -0.0866$	$C_{l_{\beta_2}} = -0.3620$	$C_{n_{\beta_0}} = 0.0885$
$C_{m_{\delta_{\text{stab}2}}} = 0.9338$	$C_{l_{\beta_1}} = -0.4153$	$C_{n_{\delta_{\text{ail}3}}} = 0.2694$
$C_{m_{\delta_{\text{stab}1}}} = -0.3245$	$C_{l_{\beta_0}} = -0.0556$	$C_{n_{\delta_{\text{ail}2}}} = -0.3413$
$C_{m_{\delta_{\text{stab}0}}} = -0.9051$	$C_{l_{\delta_{\text{ail}3}}} = 0.1989$	$C_{n_{\delta_{\text{ail}1}}} = 0.0584$
$C_{m_{q_3}} = 64.7190$	$C_{l_{\delta_{\text{ail}2}}} = -0.2646$	$C_{n_{\delta_{\text{ail}0}}} = 0.0104$
$C_{m_{q_2}} = -68.5641$	$C_{l_{\delta_{\text{ail}1}}} = -0.0516$	$C_{n_{\delta_{\text{rud}4}}} = 0.3899$
$C_{m_{q_1}} = 10.9921$	$C_{l_{\delta_{\text{ail}0}}} = 0.1424$	$C_{n_{\delta_{\text{rud}3}}} = -0.8980$
$C_{m_{q_0}} = -4.1186$	$C_{l_{\delta_{\text{rud}3}}} = -0.0274$	$C_{n_{\delta_{\text{rud}2}}} = 0.5564$
—	$C_{l_{\delta_{\text{rud}2}}} = 0.0083$	$C_{n_{\delta_{\text{rud}1}}} = -0.0176$
—	$C_{l_{\delta_{\text{rud}1}}} = 0.0014$	$C_{n_{\delta_{\text{rud}0}}} = -0.0780$
—	$C_{l_{\delta_{\text{rud}0}}} = 0.0129$	$C_{n_{p_1}} = -0.0881$
—	$C_{l_{p_1}} = 0.2377$	$C_{n_{p_0}} = 0.0792$
—	$C_{l_{p_0}} = -0.3540$	$C_{n_{r_1}} = -0.1307$
—	$C_{l_{r_2}} = -1.0871$	$C_{n_{r_0}} = -0.4326$
—	$C_{l_{r_1}} = 0.7804$	—
—	$C_{l_{r_0}} = 0.1983$	—

Table 3 Aerodynamic force coefficients

Sideforce coefficient	Drag force coefficient	Lift force coefficient
$C_{Y_{\beta_2}} = -0.1926$	$C_{D_{\alpha_4}} = 1.4610$	$C_{L_{\alpha_3}} = 1.1645$
$C_{Y_{\beta_1}} = 0.2654$	$C_{D_{\alpha_3}} = -5.7341$	$C_{L_{\alpha_2}} = -5.4246$
$C_{Y_{\beta_0}} = -0.7344$	$C_{D_{\alpha_2}} = 6.3971$	$C_{L_{\alpha_1}} = 5.6770$
$C_{Y_{\delta_{\text{ail}3}}} = -0.8500$	$C_{D_{\alpha_1}} = -0.1995$	$C_{L_{\alpha_0}} = -0.0204$
$C_{Y_{\delta_{\text{ail}2}}} = 1.5317$	$C_{D_{\alpha_0}} = -1.4994$	$C_{L_{\delta_{\text{stab}3}}} = 2.1852$
$C_{Y_{\delta_{\text{ail}1}}} = -0.2403$	$C_{D_0} = 1.5036$	$C_{L_{\delta_{\text{stab}2}}} = -2.6975$
$C_{Y_{\delta_{\text{ail}0}}} = -0.1656$	$C_{D_{\delta_{\text{stab}3}}} = -3.8578$	$C_{L_{\delta_{\text{stab}1}}} = 0.4055$
$C_{Y_{\delta_{\text{rud}3}}} = 0.9351$	$C_{D_{\delta_{\text{stab}2}}} = 4.2360$	$C_{L_{\delta_{\text{stab}0}}} = 0.5725$
$C_{Y_{\delta_{\text{rud}2}}} = -1.6921$	$C_{D_{\delta_{\text{stab}1}}} = -0.2739$	—
$C_{Y_{\delta_{\text{rud}1}}} = 0.4082$	$C_{D_{\delta_{\text{stab}0}}} = 0.0366$	—
$C_{Y_{\delta_{\text{rud}0}}} = 0.2054$	—	—

where $\kappa = I_{xx}I_{zz} - I_{xz}^2$, $l := \bar{q}SbC_l$, $M := \bar{q}ScC_M$, $n := \bar{q}SbC_n$ denote the roll, pitch and yaw moment, respectively. The moment coefficients, C_l , C_M , and C_n , are expressed as a sum of basic airframe, control deflections, and rate damping as $C_* = C_{*,\text{basic}}(\alpha, \beta) + C_{*,\text{control}}(\alpha, \delta_{\text{control}}) + C_{*,\text{rate}}(\text{rate}, V)$. The variable ‘*’ denotes l , M , n , $control$ denotes $stab$, ail , rud and $rate$ denotes the variable p , q , r . Appendix A provides explicit forms for these moment coefficients.

IV. F/A-18 Flight Control Laws

State-space realizations for both the baseline and revised flight control laws are presented in this section. This paper presents a simplified control law structure representing the stability augmentation system of the Hornet flight control system. This simplification is justified because the paper is only concerned with the stability issues of the F/A-18 aircraft. A more detailed descriptions of these flight control laws can be found in other [16,17].

The controller

$$K = \begin{bmatrix} A_c & B_c \\ C_c & D_c \end{bmatrix}$$

can be realized as the following:

$$\dot{x}_c = A_c x_c + B_c y \quad (15)$$

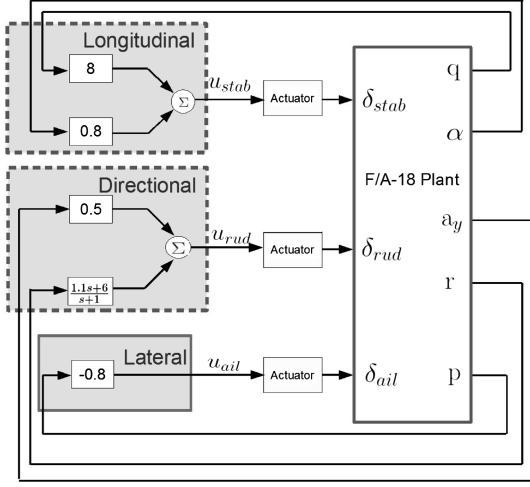


Fig. 1 F/A-18 baseline flight control law.

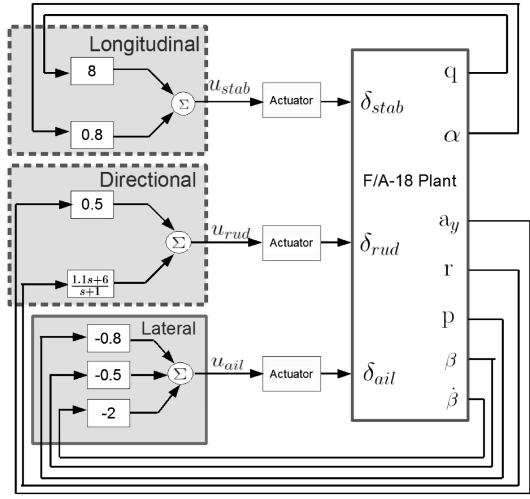


Fig. 2 F/A-18 revised flight control law.

$$u_3 = C_c x_c + D_c y \quad (16)$$

where x_c is the controller state, $u_3 := [\delta_{ail}, \delta_{rud}, \delta_{stab}]$ indicates the input of the plant. The plant measurements are $y := [a_y, p, r, \alpha, \beta, q, \dot{\beta}_{lin}]$. The lateral acceleration is given by $a_y = \frac{\dot{q} \Sigma}{mg} C_Y$ (in units of g) and computed around a flight condition. The measurement signal $\dot{\beta}_{lin}$ represents the linearized representation of the sideslip-rate ($\dot{\beta}$). This signal is estimated by using a first-order approximation to the sideslip state-derivative equation around a flight condition.

A. Realization of Baseline Flight Control Law

Figure 1 shows the simplified control law architecture for the baseline control laws used for analysis in this paper. The baseline controller structure for the F/A-18 aircraft closely follows the control augmentation system presented in the report by Buttrill et al. [36]. The actuator dynamics are ignored in the nonlinear analysis presented in this paper to reduce computational complexity. Moreover, the normal acceleration feedback, a proportional-integrator compensator in the F/A-18 baseline design, is not implemented in the simplified control law structure. The feedback gain of the normal acceleration is significantly lower at the flight condition of interest than that of alpha feedback gain. In addition, the values of normal acceleration around the flight condition of interest are estimated by performing numerous simulations. The estimated value is bounded

by 1.22 g. Hence, the contribution of the normal acceleration feedback term is negligible and eliminated from the analysis.

The state-space realization for the baseline flight control law is

$$\begin{bmatrix} A_c & B_c \\ C_c & D_c \end{bmatrix} = \begin{bmatrix} -1 & 0 & 0 & 4.9 & 0 & 0 & 0 & 0 \\ 0 & 0 & 0.8 & 0 & 0 & 0 & 0 & 0 \\ -1 & -0.5 & 0 & -1.1 & 0 & 0 & 0 & 0 \\ 0 & 0 & 0 & 0 & -0.8 & 0 & -8 & 0 \end{bmatrix} \quad (17)$$

B. Realization of Revised Flight Control Law

Figure 2 shows the architecture of the revised F/A-18 flight control law as described in the papers by Heller et al. [14,39].

The state-space realization for the revised controller is

$$\begin{bmatrix} A_c & B_c \\ C_c & D_c \end{bmatrix} = \begin{bmatrix} -1 & 0 & 0 & 4.9 & 0 & 0 & 0 & 0 \\ 0 & 0 & 0.8 & 0 & 0 & 2 & 0 & 0.5 \\ -1 & -0.5 & 0 & -1.1 & 0 & 0 & 0 & 0 \\ 0 & 0 & 0 & 0 & -0.8 & 0 & -8 & 0 \end{bmatrix} \quad (18)$$

The revised flight control law has two additional feedback measurements to the aileron and the differential stabilator channels, sideslip and sideslip-rate feedback, compared with the baseline flight control law. The paper by Heller et al. [14] refers to these additional two feedback channels, especially the sideslip-rate feedback, being the key for suppressing the falling-leaf motion.

Note, the differential stabilator channel is ignored in this paper. Both aileron and differential stabilator channels are useful to control sideslip with the ailerons being most effective to roll the aircraft at high angles-of-attack and the differential stabilator in aiding the vehicle to yaw. Since mainly roll maneuvers with small sideslip angle are considered in this paper, the differential stabilator too was deemed appropriate to ignore.

V. Polynomial Model Formulation and Validation of F/A-18 Aircraft

Section II described an approach to estimate regions of attraction for nonlinear systems. The approach to estimate lower bounds on the ROA relies on SOS optimization methods and can only be applied to polynomial systems. Moreover, the computational requirements for the SOS optimizations grow rapidly in the number of state variables and polynomial degree. This approximately limits this method to nonlinear analysis problems with at most 7–10 states and degree 3–5 polynomial models. Consequently, the construction of accurate, low-degree polynomial models is an important step in the proposed analysis process. However, to our knowledge, no rigorous method exists to construct an optimal polynomial approximation to a nonlinear dynamic system. Hence, the polynomial model in this paper is developed with an “informal” method driven by engineering judgment. In this paper, the polynomial model is formulated in two steps. First, the aerodynamic look-up data have been expressed as closed-form functions of states. Second, the closed-loop analytical nonlinear model is approximated by polynomial functions of the states by posing a least-square optimization problem over a gridded state-space region of interest. The gridded state-space region of interest is determined by the range of values the aircraft can undergo during the slow alpha falling-leaf motion. MATLAB tools has been developed to speed the development of polynomial models but this step still requires more effort when compared with the construction of linearizations. The MATLAB software to construct polynomial models is freely available at [28]. The benefit of the additional modeling effort is that the polynomial model provides information on higher-order dynamics of the vehicle that the linear models fail to capture.

This section formulates cubic degree polynomial models for the closed-loop systems consisting of the F/A-18 aircraft and the baseline and revised flight control laws.

A. Polynomial Model Formulation

A nine-state, six-DOF nonlinear model for the F/A-18 was described in Sec. III. The phugoid mode of the aircraft involves the V and θ states. The phugoid mode is slow and is not important for capturing the falling-leaf characteristics. The heading angle ψ also does not impact any of other state dynamics and hence it can be neglected. Consequently a six-state model of the F/A-18 aircraft is sufficient for analyzing the falling-leaf mode. Additional rationale for neglecting (V, θ, ψ) is discussed in [16].

The mechanism to extract a six-state representation from the nine-state model is outlined. First, the nine-state model, Eq. (11), is trimmed around a specific flight condition. The flight condition is chosen such that all three directions of the aircraft are excited. Hence, the aircraft is more likely to experience the falling-leaf motion around the flight condition.

Consider the flight condition for a coordinated turn ($\beta_t = 0^\circ$) at a 35° bank angle and at $V_t = 350$ ft/s.

The trim values are provided in Eq. (19). The subscript ' t ' denotes a trim value:

$$\begin{bmatrix} \alpha_t \\ p_t \\ q_t \\ r_t \\ \theta_t \\ \psi_t \end{bmatrix} = \begin{bmatrix} 20.17^\circ \\ -1.083^\circ/\text{s} \\ 1.855^\circ/\text{s} \\ 2.634^\circ/\text{s} \\ 18.69^\circ \\ 0^\circ \end{bmatrix}, \quad \begin{bmatrix} \delta_{\text{stab},t} \\ \delta_{\text{ail},t} \\ \delta_{\text{rud},t} \\ \delta_{\text{th},t} \end{bmatrix} = \begin{bmatrix} -4.449^\circ \\ -0.4383^\circ \\ -1.352^\circ \\ 14500 \text{ lbf} \end{bmatrix} \quad (19)$$

The analysis in this paper, is performed around the flight condition mentioned in Eq. (19). This flight condition is one of the eight operating points, specifically plant 4, around which linear analysis was performed in a previous work [16,17].

The states and inputs for the six-state model are defined relative to this trim point: $x_6 := [\beta - \beta_t, \alpha - \alpha_t, p - p_t, q - q_t, r - r_t, \phi - \phi_t]$ and $u_3 := [\delta_{\text{ail}} - \delta_{\text{ail},t}, \delta_{\text{rud}} - \delta_{\text{rud},t}, \delta_{\text{stab}} - \delta_{\text{stab},t}]$. The state derivatives for the six-state model, \dot{x}_6 , are computed using Eq. (13c), (13b), and (14) and the first row ($\dot{\phi}$ entry) of (12), respectively. In these equations, V, θ, ψ and T are held fixed at their trimmed values. Moreover, these state derivatives are linear in the inputs. Thus the six-state model is of the following form:

$$\dot{x}_6 = F(x_6) + G(x_6)u_3 \quad (20)$$

$$y = H(x_6) + J(x_6)u_3 \quad (21)$$

Figure 3 shows the structure of the closed-loop plant considered. P denotes the six-state nonlinear model mentioned in Eqs. (20) and (21). K denotes either the baseline or revised control law presented in Sec. IV. Both the closed-loop models are formed with the negative feedback of the controller (K) around the nonlinear plant (P), as shown in Fig. 3.

The autonomous ($r_{\text{ref}} = 0$) closed-loop dynamics are given by

$$\frac{dx_{\text{cl}}}{dt} = \mathcal{F}(x_{\text{cl}}) \quad (22)$$

where $x_{\text{cl}} := [x_6^T, x_c^T]^T \in \mathbb{R}^7$ denotes the closed-loop states and \mathcal{F} is given by Eq. (23):

$$\mathcal{F} = \begin{bmatrix} F(x_6) - G(x_6)C_c x_c - G(x_6)D_c M(x_6)^{-1}(H(x_6) - J(x_6)C_c x_c) + G(x_6)u_3 \\ A_c x_c + B_c M(x_6)^{-1}(H(x_6) - J(x_6)C_c x_c) \end{bmatrix} \quad (23)$$

where $M(x_6) = (I_l + J(x_6)D_c)$. l denotes the number of measurements in y .

The seven-state closed-loop model \mathcal{F} , in Eq. (23), is nonlinear due to trigonometric terms, $M(x_6)^{-1}$, and polynomial functions to model the aerodynamic coefficients. \mathcal{F} can be approximated by a third-degree polynomial function of x_{cl} . The approximation steps are as

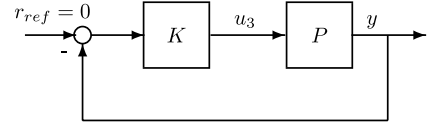


Fig. 3 Feedback system.

follows. First, the linearization of \mathcal{F} is computed at $x_{\text{cl}} = 0$. \mathcal{F} is expressed as $\mathcal{F} := \mathcal{F}_{\text{lin}}x_{\text{cl}} + \mathcal{F}_{\text{nonl}}(x_{\text{cl}})$ where \mathcal{F}_{lin} denotes the linearization. Second, each entry of the vector-valued function $\mathcal{F}_{\text{nonl}}(x_{\text{cl}})$ is approximated by a polynomial consisting of second- and third-degree terms. The benefit of this procedure is that the polynomial model retains the same linearization as the original nonlinear model.

The polynomial approximation step exploits structure that exists in the nonlinear model. For example, p, q, r , and x_c typically enter linearly with nonlinear functions of α, β , and/or ϕ . To illustrate the point, consider the state-derivative $\dot{\phi} = p + \tan \theta(q \sin \phi + r \cos \phi)$ from Eq. (12). The value of θ is held at its trim value during approximation. Notice, q and r enters linearly with nonlinear functions of ϕ . By examining each state-derivative separately, insight can be gained on the structure of the nonlinear model.

The assumed structure of the polynomial approximation used in this paper is shown while presenting the approximated closed-loop polynomial model in Appendix B. This structure is used to determine the second- and third-degree terms to include in the polynomial functions. The coefficients of the polynomial functions are computed to approximate Eq. (23) over a specified range of the closed-loop state-space. The range of the state-space is chosen to be the seven dimensional hypercube in Table 4. The state values roughly fall within the range of the slow alpha falling-leaf motion [13]. Values are provided in degrees for ease of interpretation. The hypercube is uniformly gridded along each dimension by the number of points specified in Table 4. This gridding results in a total of 60,000 samples in the hypercube. The nonlinear function $\mathcal{F}_{\text{nonl}}$ is evaluated at these points and least-squares is used to compute the polynomial coefficients that minimize the difference between $\mathcal{F}_{\text{nonl}}$ and the polynomial function at these 60,000 samples. The approximation results a cubic degree polynomial model of the form

$$\dot{x}_{\text{cl}} = \mathcal{P}(x_{\text{cl}}) \quad (24)$$

\mathcal{P} is provided in Appendix B for both the baseline and the revised controller.

B. Polynomial Model Validation

The cubic polynomial models for the baseline and revised control laws involve approximations due to neglecting three aircraft states and due to the polynomial least-squares fits. It is important to determine if the cubic polynomial models are sufficiently accurate. This section compares the polynomial closed-loop models with closed-loop models constructed with the original nine-state nonlinear model [Eq. (11)]. The term ‘‘original model’’ will refer to the closed-loop models constructed with the nine-state nonlinear model. Numerical tools do not exist to rigorously perform this comparison and hence the validation performed in this section relies

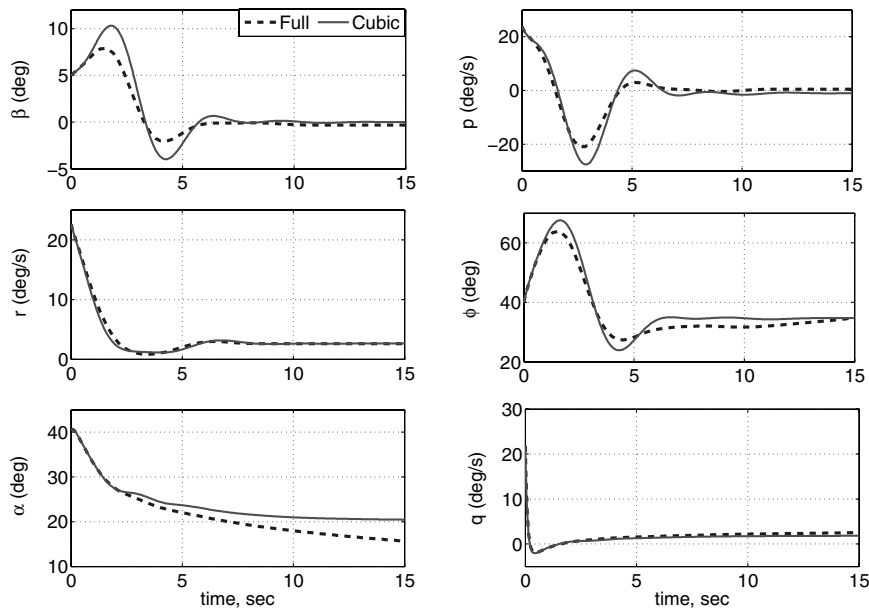
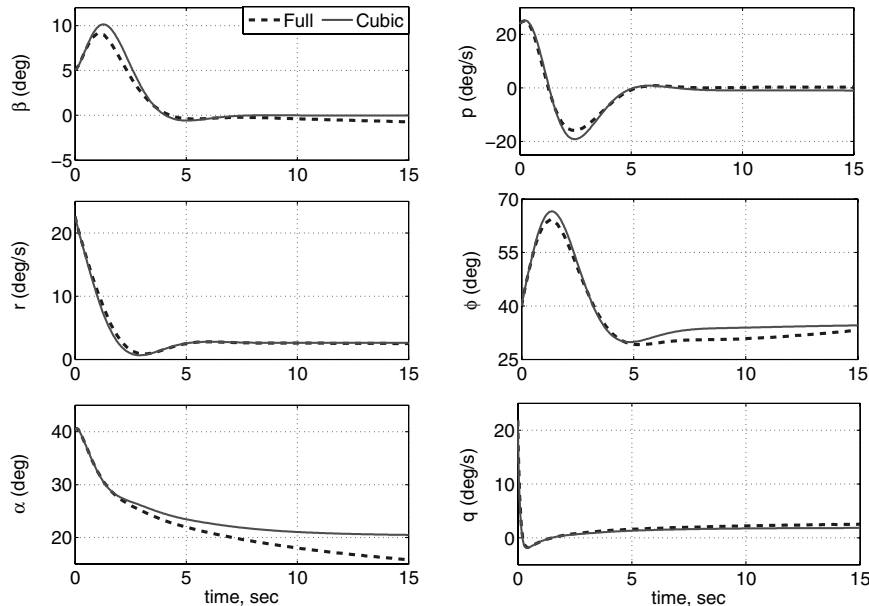
on heuristic procedures. However, the validation provides some confidence that the polynomial model provides, for engineering purposes, a sufficiently accurate approximation.

The first approach to validation is to compare the polynomial and original model by simulating from many initial conditions. Numerous simulations have been performed by perturbing the states

Table 4 State-space hypercube data for constructing polynomial models

State	Range: [min max]	Trim value	Sampled data points
β , deg	$[-10^\circ \ 10^\circ]$	0°	5
α , deg	$[-4.83^\circ \ 45.17^\circ]$	20.17°	6
p , deg/s	$[-36.083^\circ/s \ 33.91^\circ/s]$	$-1.083^\circ/s$	5
q , deg/s	$[-28.85^\circ/s \ 31.85^\circ/s]$	$1.85^\circ/s$	5
r , deg/s	$[-12.37^\circ/s \ 17.63^\circ/s]$	$2.63^\circ/s$	5
ϕ , deg	$[10^\circ \ 60^\circ]$	35°	5
x_c , deg	$[-20^\circ \ 20^\circ]$	—	4

from their trim values. Most state trajectories are similar for both the polynomial and original model. Figure 4 compares the polynomial and original models with the baseline control law. This specific simulation is performed by perturbing the β , α , p , q , r , ϕ states by 5, 20 and 25° and 20°/s, 20°/s, 5°/s, respectively, from their trim

**Fig. 4** Simulation comparison between the original and approximated closed-loop baseline models due to initial perturbation in the states.**Fig. 5** Simulation comparison between the original and approximated closed-loop revised models due to initial perturbation in the states.

points. For the original models, V , θ , and ψ are initialized to their trim values. The simulation results show that the polynomial model is in good agreement with the original model. Note, however, that the α trajectory for the polynomial model diverges from the original model as time progresses. This deviation is large (relative to other states) when the perturbation in the α state is large. However, the simulation comparisons show that the cubic degree polynomial model captures the dynamic characteristics of the original closed-loop model, even with such large perturbation in the initial condition.

Figure 5 provides a similar comparison of the polynomial and original models with the revised control law. Similar results were obtained at many other simulation initial conditions. This indicates that the polynomial approximation accurately the closed-loop dynamics of the original nonlinear closed-loop model.

The second comparison method provides a statistical quantification on the accuracy of the polynomial model approximation. The closed-loop realization for either of the controllers can be generated by using Eq. (23) based on the original nonlinear model.

For a given control law, two different seven-state realizations are developed: 1) \mathcal{F} , based on the original nonlinear model, and 2) \mathcal{P} , a cubic degree polynomial approximation to \mathcal{P} . For this comparison, both the models are evaluated by sampling random points within the ellipsoid $x_{ci}^T N x_{ci} \leq \bar{\beta}$, where $\bar{\beta}$ is the upper bound of ROA estimation introduced in Sec. II. The value of $\bar{\beta}$ for both the control law is estimated in Sec. VI.A. Moreover, the shape matrix N in the ellipsoid is presented in Eq. (25). The relative weightings of the diagonal elements of N is determined by the physical operating range of the states around the trim point specified. In other words, the shape matrix roughly scales each state by the maximum magnitude observed during the flight conditions. The maximum magnitude is chosen to be the range of states over which the least squares is performed, as mentioned in Table 4. For ease of interpretation, the shape matrix is also provided in units of degrees or deg/s. However, the computation is performed using the radian representation of N :

$$N := \text{diag}(0.1745 \text{ rad}, 0.4363 \text{ rad}, 0.6109 \text{ rad/s}, 0.5236 \text{ rad/s}, \\ 0.2618 \text{ rad/s}, 0.4363 \text{ rad}, 0.3491 \text{ rad})^{-2} \quad (25)$$

$$:= \text{diag}(10^\circ, 25^\circ, 35^\circ/\text{s}, 30^\circ/\text{s}, 15^\circ/\text{s}, 25^\circ, 20^\circ)^{-2} \quad (26)$$

Now, define relative error $:= \frac{\|\mathcal{F}|_{x_i} - \mathcal{P}|_{x_i}\|_2}{\|\mathcal{F}|_{x_i}\|_2}$, where $x_i \in \mathbb{R}^{7 \times 1}$ satisfies $x_i^T N x_i \leq \bar{\beta}$. The relative error, evaluated within the ellipsoid, defines a metric on the notion of how ‘‘close’’ the approximated model is to the original model. The relative error for the baseline control law is computed at 30,000 different $x_i \in \mathbb{R}^{7 \times 1}$ within the ellipsoid $x_i^T N x_i \leq 2.3$. Note, $\bar{\beta} = 2.3$ is taken from Sec. VI.A. The approximation incurs less than 10% relative error on 88% of the 30,000 points. Similarly, the relative error for the revised control law is also computed at 30,000 different points within the ellipsoid $x_i^T N x_i \leq 5.9$. In this case, the approximation incurs less than 10% relative error on approximately 90% of the 30,000 points. Moreover, for both the control laws, the spread of the relative error is uniform as the approximated models deviate away from the trim point.

Both validation approaches are heuristic because it is still an open problem to develop rigorous and computable metrics of the approximation error between a generic nonlinear (nonanalytic) model and a polynomial model. However, these approaches provide some confidence that the developed polynomial model has captured the dynamic characteristics of the original model, for all engineering purposes.

VI. Nonlinear Analysis

Extensive linear analyses has been performed to compare the robustness properties of the closed-loop systems with the baseline and revised flight control laws [17]. Both closed-loop systems yield similar gain and phase margins, while some of the μ analyses indicated that the revised design has better robustness properties than the baseline. However, linear analysis is only valid within a small region around the operating point which is in general insufficient for analyzing nonlinear phenomenon like the falling-leaf motion. This section applies the nonlinear ROA estimation (described in Sec. II) method to compare the robustness properties of both flight control laws. The analyses are performed for the operating point mentioned in Eq. (19) using the cubic polynomial closed-loop models developed in Sec. V.

A. Estimation of Upper Bound on ROA

The Monte Carlo search, described in Sec. II, is used to estimate ROA upper bounds $\bar{\beta}$ for both flight control laws. The Monte Carlo search was performed with 2 million simulations each for the baseline and revised control laws. The search returns an initial condition x_0 on the boundary of the ellipsoid, i.e. $p(x_0) = x_0^T N x_0 = \bar{\beta}_{MC}$, that causes the system to go unstable. Hence, the value of the $\bar{\beta}_{MC}$ provides an upper bound of the ROA for the F/A-18

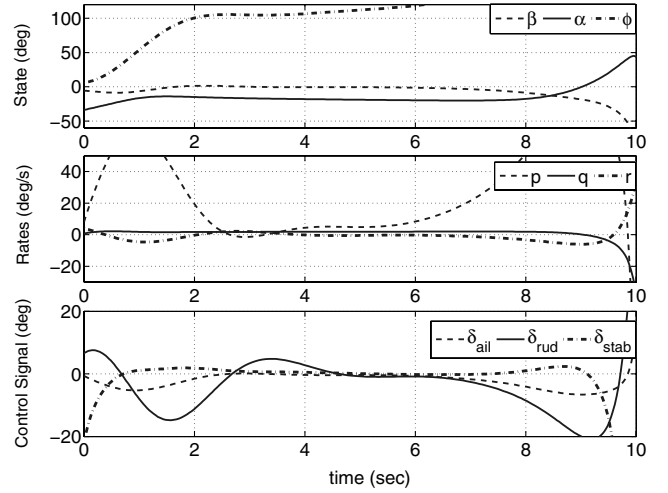


Fig. 6 Unstable trajectories for baseline control law with initial condition (IC) s.t. $x_0^T N x_0 = 2.298$.

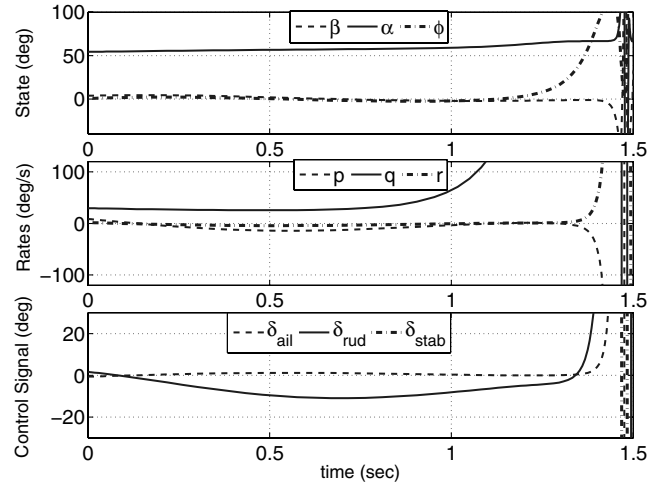


Fig. 7 Unstable trajectories for revised control law with IC s.t. $x_0^T N x_0 = 5.895$.

aircraft. Recall that the shape matrix N is defined in Eq. (25). The baseline control law provides an upper bound of $\bar{\beta}_{MC} = 2.298$ whereas the revised control law provides an upper bound of $\bar{\beta}_{MC} = 5.836$.

The Monte Carlo search returned the following initial condition for the closed system with the baseline control law:

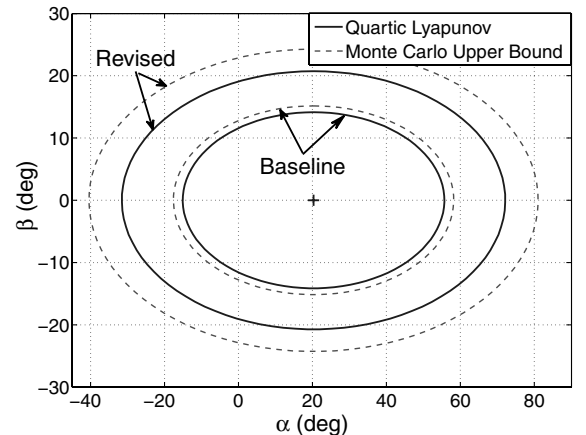


Fig. 8 Lower/upper bound slices for ROA estimate in α - β plane. The lower bound estimate is based on the quartic Lyapunov function.

$$x_0 = [-5.632^\circ, -33.54^\circ/\text{s}, 7.908^\circ/\text{s}, 0.6103^\circ, 3.959^\circ, 6.107^\circ/\text{s}, 0.06820^\circ]^T$$

This initial condition satisfies $p(x_0) = 2.298$. Figure 6 shows the unstable response of the baseline system resulting from this initial condition. Decreasing the initial condition slightly to $0.995x_0$ leads to a stable response.

For the revised control law the Monte Carlo search returned the following initial condition:

$$x_0 = [3.841^\circ, 54.25^\circ/\text{s}, 8.705^\circ/\text{s}, 29.45^\circ, 1.641^\circ, 0.630^\circ/\text{s}, 0.7880^\circ]^T$$

This initial condition satisfies $p(x_0) = 5.895$ and Fig. 7 shows the unstable response of the revised system resulting from this initial condition. Again, a stable initial condition is obtained by slightly decreasing the initial condition to $0.995x_0$.

The complete six-DOF model, including actuator dynamics and position/rate limits, was simulated with the initial condition, $x_{0,\text{poly}}$, for which the polynomial model was unstable. For both control laws the six-DOF model exhibits stable response with these initial conditions. Next, The full six-DOF model was simulated with the scaled initial condition $\zeta x_{0,\text{poly}}$. For the baseline control law, the complete six-DOF model was unstable when the initial condition was scaled by $\zeta = 1.3$. This gives an ROA upper bound estimate of $\bar{\beta}_{\text{full}} = 3.883$ for the complete six-DOF model. For the revised control law, the complete six-DOF model was unstable when the initial condition was scaled by $\zeta = 1.1$, resulting in an upper bound of $\bar{\beta}_{\text{full}} = 7.132$. For both the baseline and revised controllers, the upper bound estimation of the complete six-DOF model is slightly larger than the ones for the polynomial model.

The Monte Carlo technique described preceding can also be directly applied to the complete six-DOF model. The Monte Carlo search to the complete six-DOF model was performed with 10,000 simulations each for the baseline and revised control laws. For the baseline control law, applying the Monte Carlo method to the complete six-DOF model results in an ROA upper bound estimate of $\bar{\beta}_{\text{full}} = 2.154$. The initial condition achieving this bound is given by

$$x_0 = [-6.538^\circ, 8.198^\circ/\text{s}, 14.54^\circ/\text{s}, -3.699^\circ, 17.92^\circ, 1.472^\circ/\text{s}, 0^\circ]^T$$

For the revised control law, the ROA upper bound estimate is $\bar{\beta}_{\text{full}} = 12.00$. The initial condition is

$$x_0 = [10.65^\circ, 59.63^\circ/\text{s}, 15.55^\circ/\text{s}, -16.52^\circ, 17.88^\circ, -24.12^\circ/\text{s}, -30.45^\circ]^T$$

Note, scaling the initial conditions, that result instability in the polynomial model, provide better upper bound estimates for the complete six-DOF model.

B. Estimation of Lower Bound on ROA

The $V - s$ iteration, described in Sec. II, is employed to estimate the ROA lower bounds $\underline{\beta}$ for both the F/A-18 flight control laws. Recall, $N = N^T$ indicates the shape matrix of ellipsoid and is determined by the physical operating range of the states around the trim point specified. N is provided by Eq. (25). The ellipsoid, $x_{\text{cl}}^T N x_{\text{cl}} = \beta$, defines the set of initial conditions for which the control law will bring the aircraft back to its trim point. The state corresponding to the smaller diagonal element of N is expected to have a wide range of variation in estimating the ROA. If the aircraft is perturbed due to a wind gust or other upset condition but remains in the ellipsoid the control law will recover the vehicle back to trim. In other words, the ellipsoid defines a safe flight envelope for the F/A-18. Hence, the ROA provides a measure of how much perturbation

the aircraft can tolerate before it becomes unstable. Roughly, the value of the $\underline{\beta}$ can be thought of as ‘nonlinear stability margin’, similar to the linear stability margin (k_m) concept presented in the linear analysis [16]. However, these two margins are not directly comparable to each other.

Increasing the degree of the Lyapunov function improves the lower bound estimate of the ROA as discussed in Sec. II. At first, bounds using the quadratic Lyapunov function from linearized analysis, denoted as $\underline{\beta}_{\text{LIN}}$, are computed. This method has been proposed for validation of flight control laws [1]. The baseline flight control law achieves a bound of $\underline{\beta}_{\text{LIN}} = 5.100 \times 10^{-3}$ while the revised achieves $\underline{\beta}_{\text{LIN}} = 8.200 \times 10^{-3}$. Recall, the upper bound estimation, $\bar{\beta}_{\text{MC}}$, of the ROA is 2.298 for baseline and 5.895 for the revised flight control law. These lower bounds are not particularly useful because they are three orders of magnitude smaller than the corresponding upper bounds. The estimate of the lower bound needs to be improved. Hence, the $V - s$ iteration with quadratic and quartic Lyapunov functions are used to increase the lower bound estimate.

The $V - s$ iteration with quadratic Lyapunov functions gives $\underline{\beta}_2 = 0.8921$ for the baseline control law and $\underline{\beta}_2 = 3.719$ for the revised control law. The lower bound estimation was improved dramatically compared with the linearized Lyapunov analysis. However, the estimation can be further improved by using quartic Lyapunov function. The $V - s$ iteration with quartic Lyapunov functions is $\underline{\beta}_4 = 2.006$ for the baseline control law and $\underline{\beta}_4 = 4.299$ for the revised control law. These bounds are significantly larger than the bounds obtained for the linearized Lyapunov function. A sixth-order Lyapunov function can lead to improved lower bounds but with a significant increase in computation time. The lower bounds with different degree of Lyapunov function show that the linearized ROA

method is much more conservative than the results obtained using the quartic Lyapunov function.

Moreover, numerous initial conditions have been generated by sampling both the inner ellipsoids of the ROA. These sampled initial conditions are used to simulate the complete six-DOF model. The complete six-DOF model was stable for all initial conditions generated by this method. This provides confidence that the ROA lower bound estimate computed with the polynomial model is contained with the ROA for the complete six-DOF model.

C. Discussion

The largest ellipsoid contained in the ROA is denoted as $\mathcal{E}_{\beta^*} := \{x_{\text{cl}} \in \mathbb{R}^7: x_{\text{cl}}^T N x_{\text{cl}} \leq \beta^*\}$. The lower and upper bounds on β^* have been computed for the polynomial closed-loop systems with both F/A-18 flight control laws. The bounds on β^* for the baseline control law are: $2.006 \leq \beta^* \leq 2.298$. For the revised control law the bounds are: $4.299 \leq x_{\text{cl}}^T N x_{\text{cl}} \leq 5.895$. The same relation holds even when the outer bounds are computed with the six-DOF model. These

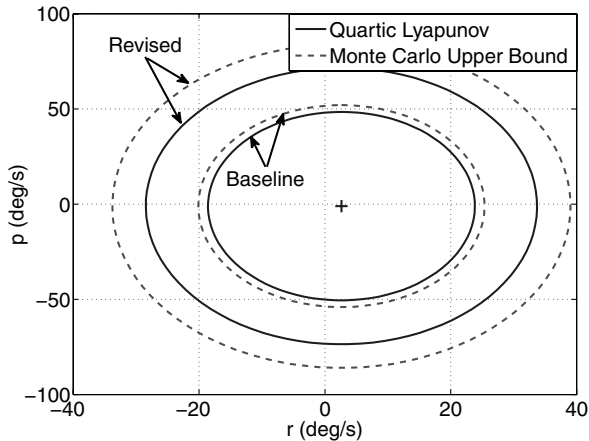


Fig. 9 Lower/upper bound slices for ROA estimate in p - r . The lower bound estimate is based on the quartic Lyapunov function.

bounds on the ROA can be visualized by plotting slices of the ellipsoid $x_{cl}^T N x_{cl}$. Figures 8 and 9 show slices of both the inner/outer approximations of the best ellipsoidal ROA approximation for both the flight control laws, respectively, in α - β and p - r planes. These states are chosen because they play an important role in characterizing the falling-leaf motion. In both the figures, the solid lines show the slices of the inner bounds obtained from quartic Lyapunov analysis. Every initial condition within the solid ellipses will return to the trim condition (marked as +). If the aircraft is perturbed due to an upset condition or wind gust but remains within this ellipsoid then the control law will recover the aircraft and bring it back to trim. The dashed lines show the slices of the outer bounds obtained from Monte Carlo analysis. There is at least one initial condition on the outer ellipsoid which leads to a divergent trajectory. The ellipsoid is seven dimensional and hence the initial condition leading to a divergent trajectory does not necessarily lie on the slice of the ellipsoid shown in the figure. Upset conditions that push the aircraft state to this upper bound ellipsoid could potentially lead to loss of control.

The closeness of these upper/lower bounds indicate that the best ellipsoidal ROA approximation problem has been solved for engineering purposes. Hence, definitive conclusions regarding the stability region about the flight control laws can be drawn for the F/A-18 aircraft. The slices for the quartic Lyapunov functions demonstrate that the ROA estimate for the revised control law is larger than the one for the baseline control law. For example, from the α - β slice it can be concluded that the baseline controller returns to the trim condition for initial perturbations in an ellipse defined by β between (approximately) -14° and $+14^\circ$ and α between (approximately) -15° and $+55^\circ$. The revised controller returns to the trim condition for initial perturbations in an ellipse defined by β between -21° and $+21^\circ$ and α between -32° and $+72^\circ$. It is important to note that, the revised controller is better able to damp out the sideslip motion and consequently, increasing the Dutch-roll damping. It has been shown that increased dutch-roll damping due to the revised flight control law architecture is one of the key reasons to suppress the falling-leaf motion [14]. Figure 8 shows that the sideslip damping has significantly improved in the revised flight control law compared with the baseline design. The stability region also increases along other state direction under the revised flight control law. Moreover, the aircraft also achieves an increased stability region along the angle-of-attack direction with the revised design. Overall, the suppression of the falling leaf can be attributed to the larger stability region provided by the revised flight control law.

In fact, the robustness improvement for the revised controller is more dramatic if the volume of the ROA estimate is considered. The volume of the ellipsoid \mathcal{E}_β is proportional to $\beta^{(n/2)}$ where $n = 7$ is the state dimension. Thus the ROA estimate obtained by the revised control law has a volume which is $(\beta_{4,rev}/\beta_{4,base})^{3.5}$ greater than that obtained by the baseline design. This corresponds to a volume increase of 14.3 for the revised flight control law. Thus information from these two ellipsoids can be used to draw conclusions about the

Table 5 Computational time for estimating lower bound of ROA with V - s iteration procedure

Plant	Lyapunov degree	Iteration steps	Baseline	Revised
—	Fourth	80	7.935 Hrs	7.365 Hrs
Seven-state, cubic degree	Second	40	0.113 Hrs	0.111 Hrs
Seven-state linear	Second	40	0.00340 Hrs	0.00440 Hrs

safe flight envelope. The size of these ellipsoids measure the robustness of the flight control law to disturbances. In summary, the ellipsoids define a metric for the safe flight envelope of the F/A-18 aircraft. Based on this metric, the revised control law has an increased safe flight envelope, which helps suppressing the falling-leaf motion.

The nonlinear analysis tools used in this paper currently cannot incorporate hard nonlinearities, e.g., actuator position and rate limits. Hence these hard nonlinearities are neglected. In addition, the actuator dynamics are neglected to reduce the computational time associated with the nonlinear analysis method. These approximations have an effect on the estimated recovery envelope. The impact of these approximations can be assessed by comparing the results with simulations on the full six-DOF model including actuator dynamics and position/rate limits. Direct incorporation of hard nonlinearities in the proposed nonlinear analysis method is currently an area of active research.

The nonlinear analysis imposes a limitation that the dynamics of the aircraft need to be described by the polynomial functions of the states. Hence, the caveat with this nonlinear analysis results is that the size of the ROA may be larger than where the polynomial model is valid. Because of the approximation procedure, the approximated polynomial model deviates from the original model away from the trim points. As a cross-validation, both the approximated and the original model are simulated by sampling the initial conditions on the ellipsoid $x_{cl}^T N x_{cl} = \beta$. Numerous simulation comparisons revealed that both the models' state trajectories are in good agreement, in light of the discussion of Sec. V.B. Moreover, the heuristic statistical method of model validation, performed in Sec. V.B, also provides some confidence on the validity of the approximated model on the boundary of the outer ellipsoidal approximation.

The computation time required for the lower bounds is summarized in Table 5. The quartic Lyapunov functions provided much better lower bounds than the quadratic Lyapunov functions. However, computing bounds with quartic Lyapunov functions required significantly more time than computing bounds with quadratic Lyapunov functions. This is due to the computational growth of SOS optimizations due to an increase in the degree of the polynomial model. Increasing the state dimension, e.g., by including the V and θ states, also would result in a large increase in computation for the lower bounds. The analyses are performed on Intel Core i7 CPU 2.67 GHz 8.00 GB RAM.

VII. Conclusions

This paper estimated bounds on the regions of attraction for 2 F/A flight control laws. Upper bounds were estimated using Monte Carlo simulations and lower bounds were estimated using SOS optimization. It is important to note that the ROA analysis accounts for significant nonlinearities in the F/A-18 aircraft dynamics. This makes the analysis more applicable to nonlinear flight phenomenon such as the falling-leaf mode. The conclusion of this analysis is that the revised F/A-18 flight control law has a significantly larger region-of-attraction than the baseline control law. This nonlinear analysis indicates that revised control law is less susceptible to a loss of control phenomenon like the falling-leaf mode.

Appendix A: Aerodynamic Coefficients

The aerodynamic coefficients presented here have been extracted from various papers [29–34]. The aerodynamic model of the aircraft

is presented here as a closed-form expression. Moreover, the MATLAB M-files to generate the models and the results shown in this paper can also be found in the website[†]:

$$\begin{aligned} \text{Pitching Moment, } C_m &= (C_{m_{\alpha_2}} \alpha^2 + C_{m_{\alpha_1}} \alpha + C_{m_{\alpha_0}}) \\ &+ (C_{m_{\delta_{\text{stab}_2}}} \alpha^2 + C_{m_{\delta_{\text{stab}_1}}} \alpha + C_{m_{\delta_{\text{stab}_0}}}) \delta_{\text{stab}} \\ &+ \frac{\bar{c}}{2V_T} (C_{m_{q_3}} \alpha^3 + C_{m_{q_2}} \alpha^2 + C_{m_{q_1}} \alpha + C_{m_{q_0}}) q \end{aligned}$$

$$\begin{aligned} \text{Rolling Moment, } C_l &= (C_{l_{\beta_4}} \alpha^4 + C_{l_{\beta_3}} \alpha^3 + C_{l_{\beta_2}} \alpha^2 + C_{l_{\beta_1}} \alpha \\ &+ C_{l_{\beta_0}}) \beta + (C_{l_{\delta_{\text{ail}_3}}} \alpha^3 + C_{l_{\delta_{\text{ail}_2}}} \alpha^2 + C_{l_{\delta_{\text{ail}_1}}} \alpha + C_{l_{\delta_{\text{ail}_0}}}) \delta_{\text{ail}} \\ &+ (C_{l_{\delta_{\text{rud}_3}}} \alpha^3 + C_{l_{\delta_{\text{rud}_2}}} \alpha^2 + C_{l_{\delta_{\text{rud}_1}}} \alpha + C_{l_{\delta_{\text{rud}_0}}}) \delta_{\text{rud}} + \frac{b}{2V_T} (C_{l_{p_1}} \alpha \\ &+ C_{l_{p_0}}) p + \frac{b}{2V_T} (C_{l_{r_2}} \alpha^2 + C_{l_{r_1}} \alpha + C_{l_{r_0}}) r \end{aligned}$$

$$\begin{aligned} \text{Yawing Moment, } C_n &= (C_{n_{\beta_2}} \alpha^2 + C_{n_{\beta_1}} \alpha + C_{n_{\beta_0}}) \beta \\ &+ (C_{n_{\delta_{\text{rud}_4}}} \alpha^4 + C_{n_{\delta_{\text{rud}_3}}} \alpha^3 + C_{n_{\delta_{\text{rud}_2}}} \alpha^2 + C_{n_{\delta_{\text{rud}_1}}} \alpha \\ &+ C_{n_{\delta_{\text{rud}_0}}}) \delta_{\text{rud}} + (C_{n_{\delta_{\text{ail}_3}}} \alpha^3 + C_{n_{\delta_{\text{ail}_2}}} \alpha^2 + C_{n_{\delta_{\text{ail}_1}}} \alpha \\ &+ C_{n_{\delta_{\text{ail}_0}}}) \delta_{\text{ail}} + \frac{b}{2V_T} (C_{n_{p_1}} \alpha + C_{n_{p_0}}) p + \frac{b}{2V_T} (C_{n_{r_1}} \alpha + C_{n_{r_0}}) r \end{aligned}$$

$$\begin{aligned} \text{Sideforce Coefficient, } C_Y &= (C_{Y_{\beta_2}} \alpha^2 + C_{Y_{\beta_1}} \alpha + C_{Y_{\beta_0}}) \beta \\ &+ (C_{Y_{\delta_{\text{ail}_3}}} \alpha^3 + C_{Y_{\delta_{\text{ail}_2}}} \alpha^2 + C_{Y_{\delta_{\text{ail}_1}}} \alpha + C_{Y_{\delta_{\text{ail}_0}}}) \delta_{\text{ail}} + (C_{Y_{\delta_{\text{rud}_3}}} \alpha^3 \\ &+ C_{Y_{\delta_{\text{rud}_2}}} \alpha^2 + C_{Y_{\delta_{\text{rud}_1}}} \alpha + C_{Y_{\delta_{\text{rud}_0}}}) \delta_{\text{rud}} \end{aligned}$$

$$\begin{aligned} \text{Lift Coefficient, } C_L &= (C_{L_{\alpha_3}} \alpha^3 + C_{L_{\alpha_2}} \alpha^2 + C_{L_{\alpha_1}} \alpha \\ &+ C_{L_{\alpha_0}}) \cos\left(\frac{2\beta}{3}\right) + (C_{L_{\delta_{\text{stab}_3}}} \alpha^3 + C_{L_{\delta_{\text{stab}_2}}} \alpha^2 + C_{L_{\delta_{\text{stab}_1}}} \alpha \\ &+ C_{L_{\delta_{\text{stab}_0}}}) \delta_{\text{stab}} \end{aligned}$$

$$\begin{aligned} \text{Drag Coefficient, } C_D &= (C_{D_{\alpha_4}} \alpha^4 + C_{D_{\alpha_3}} \alpha^3 + C_{D_{\alpha_2}} \alpha^2 + C_{D_{\alpha_1}} \alpha \\ &+ C_{D_{\alpha_0}}) \cos \beta + C_{D_0} + (C_{D_{\delta_{\text{stab}_3}}} \alpha^3 + C_{D_{\delta_{\text{stab}_2}}} \alpha^2 + C_{D_{\delta_{\text{stab}_1}}} \alpha \\ &+ C_{D_{\delta_{\text{stab}_0}}}) \delta_{\text{stab}} \end{aligned}$$

Appendix B: Closed-Loop Polynomial Model

The closed-loop cubic degree polynomial models discussed in Sec. V are presented next. Moreover, the MATLAB M-files to generate the models can also be found in the website.**

I. Baseline Polynomial Model

The cubic degree polynomial approximation for the closed-loop system with the baseline control law is

$$\begin{aligned} \dot{\beta} &= -3.978 \times 10^{-3} \alpha^3 - 2.191 \times 10^{-1} \alpha^2 \beta + 2.9427 \times 10^{-5} \alpha^2 \phi \\ &- 2.458 \times 10^{-3} \alpha \beta^2 + 5.509 \times 10^{-2} \alpha \beta \phi - 4.330 \times 10^{-5} \alpha \phi^2 \\ &+ 6.2222 \times 10^{-2} \beta^3 - 1.672 \times 10^{-2} \beta^2 \phi + 2.785 \times 10^{-3} \beta \phi^2 \\ &- 6.786 \times 10^{-3} \phi^3 + 2.708 \times 10^{-2} \alpha^2 + 2.017 \times 10^{-1} \alpha \beta \\ &- 5.323 \times 10^{-5} \alpha \phi - 2.698 \times 10^{-2} \beta^2 + 2.729 \times 10^{-2} \beta \phi \\ &- 2.747 \times 10^{-2} \phi^2 + (-3.181 \times 10^{-1} \alpha^2 + 3.466 \times 10^{-2} \beta^2 \\ &+ 9.638 \times 10^{-1} \alpha) p + (-3.634 \times 10^{-1} \alpha \beta + 2.708 \\ &\times 10^{-1} \beta) q + (4.009 \times 10^{-1} \alpha^2 - 5.344 \times 10^{-3} \beta^2 + 3.141 \\ &\times 10^{-1} \alpha) r + (2.496 \times 10^{-2} \alpha^2 - 2.630 \times 10^{-2} \beta^2 - 5.127 \\ &\times 10^{-2} \alpha) x_{c_B} + (-1.411 \times 10^{-3} \alpha + 2.314 \times 10^{-2} \beta + 3.474 \\ &\times 10^{-1} p + 7.134 \times 10^{-2} \phi - 9.225 \times 10^{-1} r + 1.406 \times 10^{-2} x_{c_B} \end{aligned}$$

$$\begin{aligned} \dot{\alpha} &= -2.139 \times 10^{-1} \alpha^3 + 7.550 \times 10^{-3} \alpha^2 \beta + 3.540 \times 10^{-2} \alpha^2 \phi \\ &- 1.846 \times 10^{-2} \alpha \beta^2 - 4.181 \times 10^{-5} \alpha \beta \phi + 1.029 \times 10^{-2} \alpha \phi^2 \\ &- 4.365 \times 10^{-3} \beta^3 - 4.154 \times 10^{-3} \beta^2 \phi - 6.8825 \times 10^{-5} \beta \phi^2 \\ &+ 1.252 \times 10^{-2} \phi^3 + 3.637 \times 10^{-1} \alpha^2 - 5.181 \times 10^{-2} \alpha \beta \\ &+ 1.364 \times 10^{-2} \alpha \phi - 2.243 \times 10^{-2} \beta^2 + 1.093 \times 10^{-4} \beta \phi \\ &- 3.648 \times 10^{-2} \phi^2 + (6.357 \times 10^{-1} \alpha \beta - 9.576 \times 10^{-1} \beta) p \\ &+ (-1.132 \alpha^2 + 1.988 \times 10^{-1} \beta^2 + 6.941 \times 10^{-1} \alpha) q \\ &+ (-7.499 \times 10^{-1} \alpha \beta - 3.619 \times 10^{-1} \beta) r + -2.299 \times 10^{-1} \alpha \\ &+ 1.870 \times 10^{-3} \beta - 4.688 \times 10^{-2} \phi + 7.259 \times 10^{-1} q \end{aligned}$$

$$\begin{aligned} \dot{p} &= -3.314 \times 10^{-2} \alpha^3 - 19.69 \alpha^2 \beta - 1.646 \times 10^{-3} \alpha \beta^2 \\ &+ 18.79 \beta^3 - 8.022 \times 10^{-2} \alpha^2 + 15.86 \alpha \beta + 1.219 \times 10^{-3} \beta^2 \\ &+ (-5.204 \times 10^{-1} \alpha^2 + 1.252 \alpha) p + (-4.737 \alpha^2 + 6.823 \\ &\times 10^{-2} \alpha) r - 8.150 \times 10^{-1} q r - 3.173 \times 10^{-2} p q \\ &+ (-2.056 \alpha^2 + 3.553 \times 10^{-2} \alpha) x_{c_B} + 4.916 \times 10^{-2} \alpha \\ &- 7.366 \beta - 9.538 \times 10^{-1} p - 3.688 \times 10^{-2} q + 1.479 r \\ &+ 6.513 \times 10^{-1} x_{c_B} \end{aligned}$$

$$\begin{aligned} \dot{q} &= 1.553 \alpha^3 - 2.174 \alpha^2 + (17.13 \alpha^2 + 4.40 \alpha) q - 1.964 \times 10^{-2} r^2 \\ &+ 9.712 \times 10^{-1} p r + 1.964 \times 10^{-2} p^2 + (-2.303 \alpha + 4.393 \\ &\times 10^{-2} p - 14.56 q - 2.026 \times 10^{-2} r) \end{aligned}$$

$$\begin{aligned} \dot{r} &= -3.196 \times 10^{-2} \alpha^3 - 1.678 \alpha^2 \beta + 1.274 \times 10^{-2} \alpha \beta^2 - 3.236 \\ &\times 10^{-1} \beta^3 + 3.869 \times 10^{-2} \alpha^2 - 1.795 \alpha \beta - 9.442 \times 10^{-3} \beta^2 \\ &+ (-9.543 \times 10^{-2} \alpha^2 + 2.081 \times 10^{-2} \alpha) p + (-5.179 \\ &\times 10^{-1} \alpha^2 + 4.541 \times 10^{-1} \alpha) r + 3.173 \times 10^{-2} q r - 7.543 \\ &\times 10^{-1} p q + (-5.102 \times 10^{-1} \alpha^2 + 4.497 \times 10^{-1} \alpha) x_{c_B} \\ &+ -1.329 \times 10^{-2} \alpha + 5.164 \times 10^{-1} \beta + 5.438 \times 10^{-3} p \\ &+ 1.579 \times 10^{-2} q - 5.042 \times 10^{-1} r - 3.129 \times 10^{-1} x_{c_B} \end{aligned}$$

[†]Data available online at <http://www.aem.umn.edu/~AerospaceControl/> [retrieved 10 Oct. 2010].

**Data available online at <http://www.aem.umn.edu/AerospaceControl/> [retrieved 10 Oct. 2010].

$$\dot{\phi} = (-1.481 \times 10^{-1} \phi^2 + 2.921 \times 10^{-1} \phi)q + (-7.226 \times 10^{-2} \phi^2 - 2.181 \times 10^{-1} \phi)r + p + 1.941 \times 10^{-1} q + 2.772 \times 10^{-1} r$$

$$\dot{x}_{c_B} = 4.900r - x_{c_B}$$

II. Revised Polynomial Model

The cubic degree polynomial approximation for the closed-loop system with the revised control law is

$$\begin{aligned} \dot{\beta} = & 3.153 \times 10^{-6} \alpha^3 - 2.065 \times 10^{-1} \alpha^2 \beta + 1.958 \times 10^{-3} \alpha^2 \phi \\ & - 1.360 \times 10^{-3} \alpha \beta^2 + 5.556 \times 10^{-2} \alpha \beta \phi - 4.814 \times 10^{-4} \alpha \phi^2 \\ & + 5.772 \times 10^{-2} \beta^3 - 1.964 \times 10^{-2} \beta^2 \phi + 3.563 \times 10^{-3} \beta \phi^2 \\ & - 6.644 \times 10^{-3} \phi^3 + 2.404 \times 10^{-2} \alpha^2 + 1.717 \times 10^{-1} \alpha \beta \\ & - 6.328 \times 10^{-3} \alpha \phi - 2.454 \times 10^{-2} \beta^2 + 2.606 \times 10^{-2} \beta \phi \\ & - 2.771 \times 10^{-2} \phi^2 + (-3.010 \times 10^{-1} \alpha^2 + 2.034 \times 10^{-2} \beta^2 \\ & + 9.247 \times 10^{-1} \alpha)p + (-3.634 \times 10^{-1} \alpha \beta + 2.708 \\ & \times 10^{-1} \beta)q + (3.558 \times 10^{-1} \alpha^2 + 3.255 \times 10^{-2} \beta^2 + 4.181 \\ & \times 10^{-1} \alpha)r + (2.576 \times 10^{-2} \alpha^2 - 2.700 \times 10^{-2} \beta^2 - 5.287 \\ & \times 10^{-2} \alpha)x_{c_R} - 1.434 \times 10^{-3} \alpha + 2.750 \times 10^{-2} \beta + 3.529 \\ & \times 10^{-1} p + 7.253 \times 10^{-2} \phi - 9.372 \times 10^{-1} r + 1.429 \times 10^{-2} x_{c_R} \end{aligned}$$

$$\begin{aligned} \dot{\alpha} = & -2.139 \times 10^{-1} \alpha^3 + 7.550 \times 10^{-3} \alpha^2 \beta + 3.540 \times 10^{-2} \alpha^2 \phi \\ & - 1.845 \times 10^{-2} \alpha \beta^2 - 4.182 \times 10^{-5} \alpha \beta \phi + 1.029 \times 10^{-2} \alpha \phi^2 \\ & - 4.365 \times 10^{-3} \beta^3 - 4.154 \times 10^{-3} \beta^2 \phi - 6.883 \times 10^{-5} \beta \phi^2 \\ & + 1.252 \times 10^{-2} \phi^3 + 3.637 \times 10^{-1} \alpha^2 - 5.181 \times 10^{-2} \alpha \beta \\ & + 1.364 \times 10^{-2} \alpha \phi - 2.243 \times 10^{-2} \beta^2 + 1.093 \times 10^{-4} \beta \phi \\ & - 3.649 \times 10^{-2} \phi^2 + (6.357 \times 10^{-1} \alpha \beta - 9.576 \times 10^{-1} \beta)p \\ & + (-1.132 \alpha^2 + 1.988 \times 10^{-1} \beta^2 + 6.941 \times 10^{-1} \alpha)q \\ & + (-7.499 \times 10^{-1} \alpha \beta - 3.619 \times 10^{-1} \beta)r + -2.299 \times 10^{-1} \alpha \\ & + 1.871 \times 10^{-3} \beta - 4.688 \times 10^{-2} \phi + 7.259 \times 10^{-1} q \end{aligned}$$

$$\begin{aligned} \dot{p} = & -4.415 \times 10^{-1} \alpha^3 - 23.22 \alpha^2 \beta - 7.476 \times 10^{-1} \alpha^2 \phi - 2.556 \\ & \times 10^{-1} \alpha \beta^2 + 20.20 \beta^3 + 2.031 \times 10^{-1} \alpha^2 + 20.65 \alpha \beta \\ & + 1.149 \alpha \phi + 6.667 \times 10^{-2} \beta^2 + (-5.104 \alpha^2 + 7.496 \alpha)p \\ & + (7.453 \alpha^2 - 16.52 \alpha)r - 3.173 \times 10^{-2} p q - 8.151 \\ & \times 10^{-1} q r + (-2.227 \alpha^2 + 2.823 \times 10^{-1} \alpha)x_{c_R} + 6.123 \\ & \times 10^{-2} \alpha - 9.701 \beta - 3.923 p - 6.103 \times 10^{-1} \phi - 3.688 \\ & \times 10^{-2} q + 9.365 r + 5.311 \times 10^{-1} x_{c_R} \end{aligned}$$

$$\begin{aligned} \dot{q} = & 1.554 \alpha^3 - 2.175 \alpha^2 + (17.13 \alpha^2 + 4.404 \alpha)q + 1.964 \\ & \times 10^{-2} p^2 - 1.964 \times 10^{-2} r^2 + 9.713 \times 10^{-1} p r + -2.303 \alpha \\ & + 4.393 \times 10^{-2} p - 14.55 q - 2.026 \times 10^{-2} r \end{aligned}$$

$$\begin{aligned} \dot{r} = & -2.469 \times 10^{-1} \alpha^3 - 2.324 \alpha^2 \beta + 9.538 \times 10^{-2} \alpha \beta^2 - 4.018 \\ & \times 10^{-2} \beta^3 + 1.781 \times 10^{-1} \alpha^2 - 1.419 \alpha \beta - 2.519 \times 10^{-2} \beta^2 \\ & + (-9.357 \times 10^{-1} \alpha^2 + 5.264 \times 10^{-1} \alpha)p + (1.7156 \alpha^2 \\ & - 8.8988 \times 10^{-1} \alpha)r + 3.173 \times 10^{-2} q r - 7.544 \times 10^{-1} p q \\ & + (-5.427 \times 10^{-1} \alpha^2 + 4.694 \times 10^{-1} \alpha)x_{c_R} + (-1.344 \\ & \times 10^{-2} \alpha + 5.455 \times 10^{-1} \beta + 4.254 \times 10^{-2} p + 7.624 \\ & \times 10^{-3} \phi + 1.579 \times 10^{-2} q - 6.027 \times 10^{-1} r - 3.114 \times 10^{-1} x_{c_R}) \end{aligned}$$

$$\dot{\phi} = (-1.481 \times 10^{-1} \phi^2 + 2.921 \times 10^{-1} \phi)q + (-7.226 \times 10^{-2} \phi^2 - 2.182 \times 10^{-1} \phi)r + p + 1.941 \times 10^{-1} q + 2.772 \times 10^{-1} r$$

$$\dot{x}_{c_R} = 4.900r - x_{c_R}$$

Acknowledgments

This research was partially supported under the NASA Langley NASA Research Announcement contract NNH077ZEA001N entitled "Analytical Validation Tools for Safety Critical Systems." The technical contract monitor was Christine Belcastro. We would like to thank John V. Foster at NASA Langley for providing insight into the simulation modeling of the F/A-18 aircraft. We would also like to thank Ufuk Topcu at California Institute of Technology and Andrew Packard at University of California at Berkeley for many useful discussions. We would also like to thank the reviewers and the editors for their insightful comments, which have strengthened the paper.

References

- [1] Heller, M., Niewoehner, R., and Lawson, P. K., "On the Validation of Safety Critical Aircraft Systems, Part 1: An Overview of Analytical and Simulation Methods," AIAA Paper 2003-5559, 2003.
- [2] Tan, W., "Nonlinear Control Analysis and Synthesis Using Sum-of-Squares Programming," Ph.D. Thesis, Univ. of California, Berkeley, CA, 2006.
- [3] Topcu, U., Packard, A., Seiler, P., and Wheeler, T., "Stability Region Analysis Using Simulations and Sum-Of-Squares Programming," *Proceedings of the American Control Conference*, 2007, pp. 6009–6014.
- [4] Topcu, U., Packard, A., and Seiler, P., "Local Stability Analysis Using Simulations and Sum-Of-Squares Programming," *Automatica*, Vol. 44, No. 10, 2008, pp. 2669–2675. doi:10.1016/j.automatica.2008.03.010
- [5] Chiang, H.-D., and Thorp, J., "Stability Regions of Nonlinear Dynamic Systems: A Constructive Methodology," *IEEE Transactions on Automatic Control*, Vol. 34, No. 12, 1989, pp. 1229–1241. doi:10.1109/9.40768
- [6] Davison, E., and Kurak, E., "A Computational Method for Determining Quadratic Lyapunov Functions for Nonlinear Systems," *Automatica*, Vol. 7, No. 5, 1971, pp. 627–636. doi:10.1016/0005-1098(71)90027-6
- [7] Genesio, R., Tartaglia, M., and Vicino, A., "On the Estimation of Asymptotic Stability Regions: State of the Art and New Proposals," *IEEE Transactions on Automatic Control*, Vol. 30, No. 8, 1985, pp. 747–755. doi:10.1109/TAC.1985.1104057
- [8] Tibken, B., "Estimation of the Domain of Attraction for Polynomial Systems via LMIS," *Proceedings of the IEEE Conference on Decision and Control*, 2000, pp. 3860–3864.
- [9] Tibken, B., and Fan, Y., "Computing the Domain of Attraction for Polynomial Systems via BMI Optimization Methods," *Proceedings of the American Control Conference*, 2006, pp. 117–122.
- [10] Vannelli, A., and Vidyasagar, M., "Maximal Lyapunov Functions and Domains of Attraction for Autonomous Nonlinear Systems," *Automatica*, Vol. 21, No. 1, 1985, pp. 69–80. doi:10.1016/0005-1098(85)90099-8

- [11] Parrilo, P., "Structured Semidefinite Programs and Semialgebraic Geometry Methods in Robustness and Optimization," Ph.D. Thesis, California Inst. of Technology, Pasadena, CA, 2000.
- [12] Prajna, S., Papachristodoulou, A., Seiler, P., and Parrilo, P. A., *SOSTOOLS: Sum of Squares Optimization Toolbox for MATLAB*, 2004, <http://www.mit.edu/~parrilo/sostools/> [retrieved 10 Oct. 2010].
- [13] Jaramillo, P. T., and Ralston, J. N., "Simulation of the F/A-18D Falling Leaf," *AIAA Atmospheric Flight Mechanics Conference*, 1996, pp. 756–766.
- [14] Heller, M., David, R., and Holmberg, J., "Falling Leaf Motion Suppression in the F/A-18 Hornet with Revised Flight Control Software," *AIAA Paper* 2004-542, 2004.
- [15] Heller, M., Holmberg, J., and David, R. P., "Significance of Unsteady Aerodynamic Effects in F/A-18C/D Pitching Moment," *AIAA Paper* 2006-6485, 2006.
- [16] Chakraborty, A., Seiler, P., and Balas, G., "Susceptibility of F/A-18 Flight Controllers to the Falling Leaf Mode: Linear Analysis," *Journal of Guidance, Control, and Dynamics*, Vol. 34, No. 1, 2011, pp. 57–72. doi:10.2514/5.0674
- [17] Chakraborty, A., "Linear and Nonlinear Analysis of Susceptibility of F/A-18 Flight Control Laws to the Falling Leaf Mode," Master's Thesis, Univ. of Minnesota, Minneapolis, MN, 2010.
- [18] Jarvis-Wloszek, Z., "Lyapunov Based Analysis and Controller Synthesis for Polynomial Systems Using Sum-of-Squares Optimization," Ph.D. Thesis, Univ. of California, Berkeley, CA, 2003.
- [19] Jarvis-Wloszek, Z., Feeley, R., Tan, W., Sun, K., and Packard, A., "Some Controls Applications of Sum of Squares Programming," *Proceedings of the 42nd IEEE Conference on Decision and Control*, Vol. 5, 2003, pp. 4676–4681.
- [20] Tan, W., and Packard, A., "Searching for Control Lyapunov Functions Using Sums of Squares Programming," *42nd Annual Allerton Conference on Communications, Control and Computing*, 2004, pp. 210–219.
- [21] Jarvis-Wloszek, Z., Feeley, R., Tan, W., Sun, K., and Packard, A., *Positive Polynomials in Control*, Lecture Notes in Control and Information Sciences, Vol. 312, Springer-Verlag, New York, 2005, pp. 3–22.
- [22] Khalil, H., *Nonlinear Systems*, 2nd ed., Prentice-Hall, Upper Saddle River, NJ, 1996, Chap. 8.
- [23] Vidyasagar, M., *Nonlinear Systems Analysis*, 2nd ed., Prentice-Hall, Upper Saddle River, NJ, 1993, Chap. 4.
- [24] Hauser, J., and Lai, M., "Estimating Quadratic Stability Domains by Nonsmooth Optimization," *Proceedings of the American Control Conference*, 1992, pp. 571–576.
- [25] Hachicho, O., and Tibken, B., "Estimating Domains of Attraction of a Class of Nonlinear Dynamic Systems with LMI Methods Based on the Theory of Moments," *Proceedings of the IEEE Conference on Decision and Control*, 2002, pp. 3150–3155.
- [26] Lofberg, J., "YALMIP: A Toolbox for Modeling and Optimization in MATLAB," *Proceedings of the CACSD Conference*, Taipei, Taiwan, 2004.
- [27] Sturm, J., "Using SeDuMi 1.02, a MATLAB Toolbox for Optimization over Symmetric Cones," *Optimization Methods and Software*, Vols. 11–12, 1999, pp. 625–653. doi:10.1080/10556789908805766
- [28] Balas, G., Packard, A., Seiler, P., and Topcu, U., "Robustness Analysis of Nonlinear Systems," <http://www.aem.umn.edu/~AerospaceControl/> [retrieved 10 Oct. 2010].
- [29] Napolitano, M. R., Paris, A. C., and Seanor, B. A., "Estimation of the Longitudinal Aerodynamic Parameters from Flight Data for the NASA F/A-18 HARV," *AIAA Atmospheric Flight Mechanics Conference*, 1996, pp. 469–478; also *AIAA Paper* 96-3419-CP.
- [30] Napolitano, M. R., Paris, A. C., and Seanor, B. A., "Estimation of the Lateral-Directional Aerodynamic Parameters from Flight Data for the NASA F/A-18 HARV," *AIAA Atmospheric Flight Mechanics Conference*, 1996, pp. 479–489; also *AIAA Paper* 96-3420-CP.
- [31] Lluch, C. D., "Analysis of the Out-of-Control Falling Leaf Motion Using a Rotational Axis Coordinate System," Master's Thesis, Virginia Polytechnic Inst. and State Univ., Blacksburg, VA, 1998.
- [32] Iliff, K. W., and Wang, K.-S. C., "Extraction of Lateral-Directional Stability and Control Derivatives for the Basic F-18 Aircraft at High Angles of Attack," *NASA TM-4786*, 1997.
- [33] Napolitano, M. R., and Spagnuolo, J. M., "Determination of the Stability and Control Derivatives of the F/A-18 HARV from Flight Data Using the Maximum Likelihood Method," *NASA CR-193499*, 1993.
- [34] Carter, B. R., "Time Optimization of High Performance Combat Maneuvers," Master's Thesis, Naval Postgraduate School, Monterey, CA, 2005.
- [35] Stevens, B., and Lewis, F., *Aircraft Control and Simulation*, Wiley, New York, 1992, Chap. 2.
- [36] Buttrill, S. B., Arbuckle, P. D., and Hoffer, K. D., "Simulation Model of a Twin-Tail, High Performance Airplane," *NASA TR NASA TM-107601*, 1992.
- [37] Stengel, R., *Flight Dynamics*, Princeton Univ. Press, Princeton, NJ, 2004, Chap. 3.
- [38] Cook, M., *Flight Dynamics Principles*, Wiley, New York, 1997, Chap. 4.
- [39] Heller, M., Niewoehner, R., and Lawson, P. K., "High Angle of Attack Control Law Development and Testing for the F/A-18E/F Super Hornet," *AIAA Guidance, Navigation, and Control Conference*, 1999, pp. 541–551; also *AIAA Paper* 1999-4051.